Biomedical Engineering Letters (2022) 12:85–95
https://doi.org/10.1007/s13534-022-00215-1

ORIGINAL ARTICLE

A time-based single transmission-line readout with position multiplexing

Minseok Yi[1,2,3] · **Jae Sung Lee**[1,2,3,4,5]

Received: 26 November 2021 / Revised: 28 December 2021 / Accepted: 3 January 2022 / Published online: 17 January 2022

Abstract
We developed a time-based single-transmission-line readout method for time-of-flight positron emission tomography (PET) detectors. The 2D position of a silicon photomultiplier (SiPM) array was encoded in the upper and lower widths of a specially prepared L-shaped tag pulse followed by the original scintillation signal. A PET detector setup was configured using a 4 × 4 array of LSO crystals optically coupled one-to-one to a 4 × 4 SiPM array. Two pulse width modulator circuits were employed per SiPM anode signal channel and a total of 32 width-modulated digital pulses were summed and merged with a delayed common-cathode signal. The final output was analyzed using timestamps crossing two-level threshold voltages. All 16 crystals were clearly separated on a positioning map. The average energy and coincidence time resolutions were 15.0 ± 1.1% and 288.7 ± 29.3 ps after proper correction process, respectively. A 3D position decoding capability was also shown by the remarkable discrimination performance in a phoswich PET detector setup (LSO and LGSO), resulting from well-preserved scintillation signals. The proposed method enables a time-based single-channel readout with 3D gamma ray interaction position decoding capability without compromising on detector performance. This method provides gamma ray energy and arrival time information as well as 2D and depthwise interaction positions of the phoswich detectors through one channel readout. Thus, channels can be reduced by at least 4–5 times compared to typically employed charge-sharing-based position multiplexing method; this significantly reduces the burden of data acquisition on the PET system.

Keywords SiPM (silicon photomultiplier) · TOF-PET · Position multiplexing · Depth-of-interaction

1 Introduction

Silicon photomultipliers (SiPMs) are widely used semiconductor photosensors in positron emission tomography (PET) owing to their compactness, low power consumption, high gain and magnetic resonance imaging (MRI) compatibility [1–9]. Particularly, the compact size of SiPM enables one-to-one optical coupling with scintillation crystals to improve scintillation light collection efficiency, consequently offering optimal energy resolution and time-of-flight measurement performance of PET detector modules [10–15]. Accurate energy estimation allows efficient rejection or recovery of scatter events and accurate timing information is important for better image quality in TOF-PET scanners. Moreover, by individually reading the electrical signals from each SiPM, the degree of freedom in the output signal analysis increases, thus yielding its optimal performance [16–21]. However, there exist several technical barriers to implementing PET scanner systems by acquiring each signal from each SiPM individually. Massive amounts of heat generated from power-intensive active components and square-proportionally increasing (N^2; where N is the number of SiPMs in one direction) data acquisition systems will degrade the SiPM performance without a proper cooling system. Additionally,

✉ Jae Sung Lee
jaes@snu.ac.kr

1 Interdisciplinary Program in Bioengineering, Seoul National University College of Engineering, Seoul 03080, South Korea

2 Department of Nuclear Medicine, Seoul National University College of Medicine, Daehak-ro, 101, Jongno-gu, Seoul 03080, South Korea

3 Integrated Major in Innovative Medical Science, Seoul National Graduate School, Seoul, South Korea

4 Interdisciplinary Institute of Radiation Medicine, Medical Research Center, Seoul National University, Seoul, South Korea

5 Brightonix Imaging Inc., Seoul 04782, South Korea

the PET scanner must meet spatial constraints when it is inserted into an MRI scanner for PET/MRI compatibility.

Therefore, various signal multiplexing methods were investigated to enable detector scale-up with minimal performance degradation. A row-sum/column-sum readout reduces the readout channel number from N^2 to 2N by symmetrically dividing the charge generated from the SiPMs. It enables uniform energy and timing performance over the detector and high signal-to-noise ratio (SNR); however, the number of readouts increases linearly with the number of channels [22–27]. Another widely used approach is the charge division circuit, where the readout channel can be scaled down to a constant number, 4 or 5, depending on whether an additional channel is allocated for the timing signal. The most commonly employed resistive charge division circuits offer preferable crystal positioning accuracy owing to their simplicity [28–30]. However, a large RC product due to the resistive network and intrinsic capacitance of SiPM significantly reduces the detector timing performance. The capacitive charge division circuit provides better detector timing performance with no delay issue [31, 32], but it suffers from an undershooting problem of the output signal which degrades energy estimation or pulse shape discrimination. Furthermore, the aforementioned signal multiplexing methods require the use of charge-measurement devices such as charge-to-time converters (QTCs) or free-running analog-to-digital converters (ADCs). These additional active components or circuit stages lead to additional power consumption.

An alternative cost- and power-efficient approach for signal digitization is the time-over-threshold (TOT) method. In the TOT method, pulse amplitude information is encoded in the temporal width of the scintillation pulse which can then be measured using a time-to-digital converter (TDC) implemented in a field-programmable gate array (FPGA) or a simple counter circuit [33, 34]. Such signal digitization methods are referred to as time-based readouts. Further, circuit simplicity is a strong advantage of the TOT method. The TOT method, nonetheless, loses pulse shape information which provides depth-of-interaction (DOI) information [35]. The pulse shape information helps to distinguish multilayered crystals with different decay time constants in phoswich PET detectors [36–39]. The trade-off between the timing performance and noise robustness of energy estimation is also an intrinsic drawback of the TOT method.

Recently, several variations of the TOT method such as the dual-TOT, dynamic TOT, sawtooth TOT and multi-voltage threshold (MVT) method [40–47] have been investigated to overcome the drawbacks of the original TOT. Particularly, the dual-threshold TOT method maintains a low circuit complexity of the original TOT simply using two reference voltage discriminators while reducing the trade-off between the noise robustness at the scintillation signal tail and energy linearity. Additionally, it is capable of discriminating pulse shapes with decay time constant values derived from two different threshold levels and time stamps.

Collaboration of the various TOT methods and the above-mentioned signal multiplexing methods enabled both efficient signal digitization and readout channel reduction. However, still because the scintillation signal itself contains gamma ray energy and timing information but not the interaction position information, the number of readout channels is limited by the multiplexing stage. In this study, we propose a fully time-based single-channel readout method applicable to one-to-one coupled SiPM detectors with position multiplexing. This method offers gamma ray energy and arrival time information as well as 2D and depthwise interaction position of the phoswich detectors through a one-channel time-based readout without compromising the decoding performance, which implies at least four- to five-fold channel reduction compared to the typically used charge-sharing-based position multiplexing method.

2 Materials and methods

2.1 Concept

We conducted a previous position multiplexing study where in a 2D gamma ray incident position was encoded in the width and height of the pulse signal preceding a scintillation signal [48]. The capability of significant readout channel reduction was well-proven without timing performance degradation. However, the amplitude measurement of a short pulse requires an ADC operating at a high sampling speed, leaving room for improving the cost- and power efficiency. Therefore, in this study, a specially prepared L-shaped tag pulse signal was added prior to the scintillation signal. This tag pulse contains the 2-dimensional (x, y) position information of the interaction crystal in its top and bottom widths, eliminating the need for charge measurement and enabling TDC-only data acquisition. Threshold voltages of two different levels were applied to acquire the pulse width information from the crossing points. The arrival time of the gamma ray was also encoded at the rising edge of the pulse signal. The original scintillation signal was kept intact behind the tag pulse and dual-threshold voltages were applied to this scintillation signal also, thereby offering energy and decay time information. The general concept of the proposed concept is illustrated in Fig. 1.

2.2 Circuit implementation

As shown in Fig. 2, cathode signals from all the 16 SiPM pixels were bound to a common node (common-cathode signal) and tenfold pre-amplified using an ultrahigh-speed current feedback amplifier (AD8000; Analog Devices, US). The

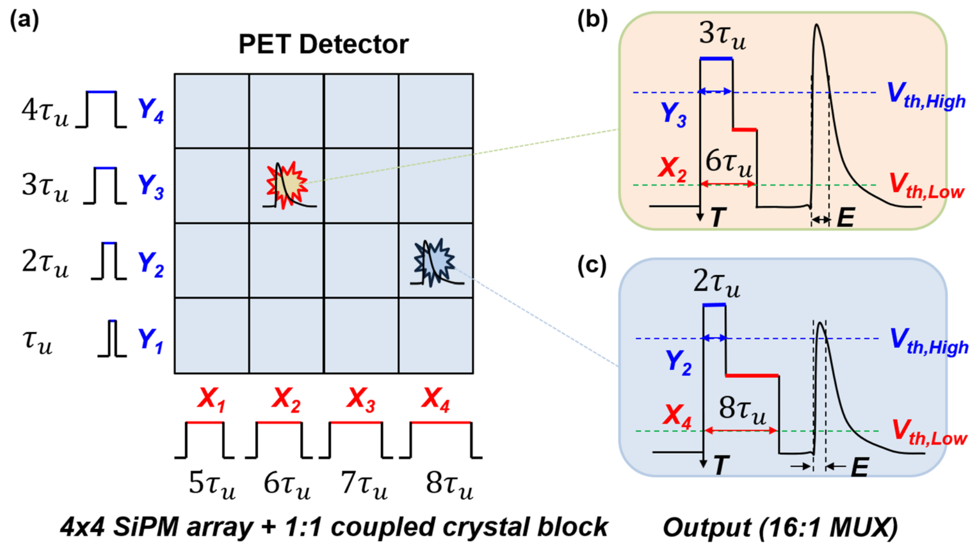

Fig. 1 Concept of Idea **a** 4×4 SiPM array **b** Circuit output when gamma ray interacted at position (X_2, Y_3) **c** Circuit output when gamma ray interacted at position (X_4, Y_2)

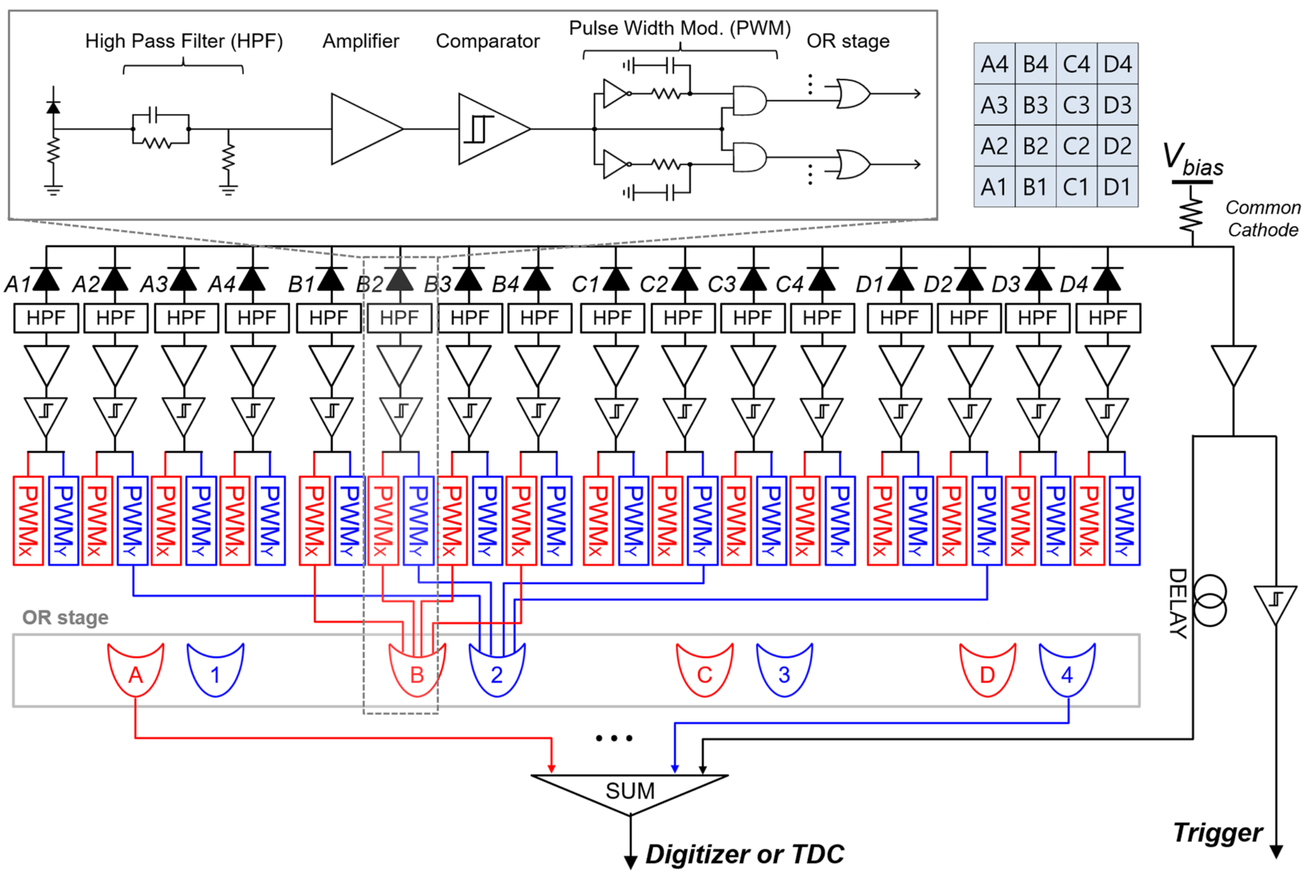

Fig. 2 Circuit implementation

amplified common cathode signal was then branched off into two routes. One of the branched lines went through a delay line that provided a sufficient signal delay to prevent the scintillation signal from interfering with the L-shaped tag pulse. The other branch of the amplified common-cathode signal was used to generate a trigger signal through a fast comparator (ADCMP601; Analog Devices, US) and a false event discriminator (FED) circuit. Individual anode signals were fed into the high-pass filters (HPFs) and preamplifiers for time jitter reduction. Subsequently, the fast SiPM anode signals were passed through the leading-edge discriminators to generate digital pulses for the signals exceeding a preset threshold voltage. The digital pulses were fed into the x- and y-position pulse width modulators (PWM_X and PWM_Y) that adjusted the pulse width according to the time constant (Rw·Cw) values. Then, the width-modulated pulse outputs were merged in the row and column directions using OR-gates. Finally, the eight OR gate outputs corresponding to each row or column and the delayed common-cathode signal were combined into a single transmission line output through a summing stage.

2.3 Data acquisition setup

2.3.1 Block detector configuration and coincidence acquisition setup

The block detector used in the coincidence study consisted of an array-type 4 × 4 SiPM (S14161-3050HS-04; Hamamatsu Photonics K.K., Japan) with a sensor pitch of 3.2 mm. The SiPM array was one-to-one optically coupled to a 4 × 4 (lutetium oxyorthosilicate (LSO) crystal array (3 mm × 3 mm × 20 mm, 3.2 mm pitch), whose pixel and pitch sizes were identical to those of the SiPM array. All crystals were optically isolated from each other by enhanced specular reflectors (ESR; > 98% reflectance, 0.065 mm thickness; 3 M). An optical grease (BC-630; Saint-Gobain, France) with a refractive index of 1.465 was used to couple the crystal array with the SiPMs. The SiPM array was operated at the bias voltage of 40.9 V which corresponded to an over voltage of 2.7 V.

Coincidence event data were acquired between the constructed block detector and a reference detector based on a photomultiplier tube (PMT) as illustrated in Fig. 3a. The output signal from the reference detector was fed into the N842 constant fraction discriminator module (CAEN S.p.A, Viareggio, Italy) and logically AND-ed with the SiPM array trigger signal using the N455 AND module (CAEN S.p.A, Viareggio, Italy) in order to generate the digitizer trigger signal. All signals were digitized with a 16-channel high-speed waveform digitizer (DT5742B; CAEN S.p.A, Viareggio, Italy) which is based on Domino Ring Sampler 4 (DRS4). Data acquisition was done with 1 GSPS sampling rate with a 12-bit sampling resolution.

2.3.2 Phoswich detector acquisition setup

A phoswich crystal detector setup was evaluated to demonstrate the depth-of-interaction (DOI) measurement capability. The phoswich crystal was constructed by stacking a

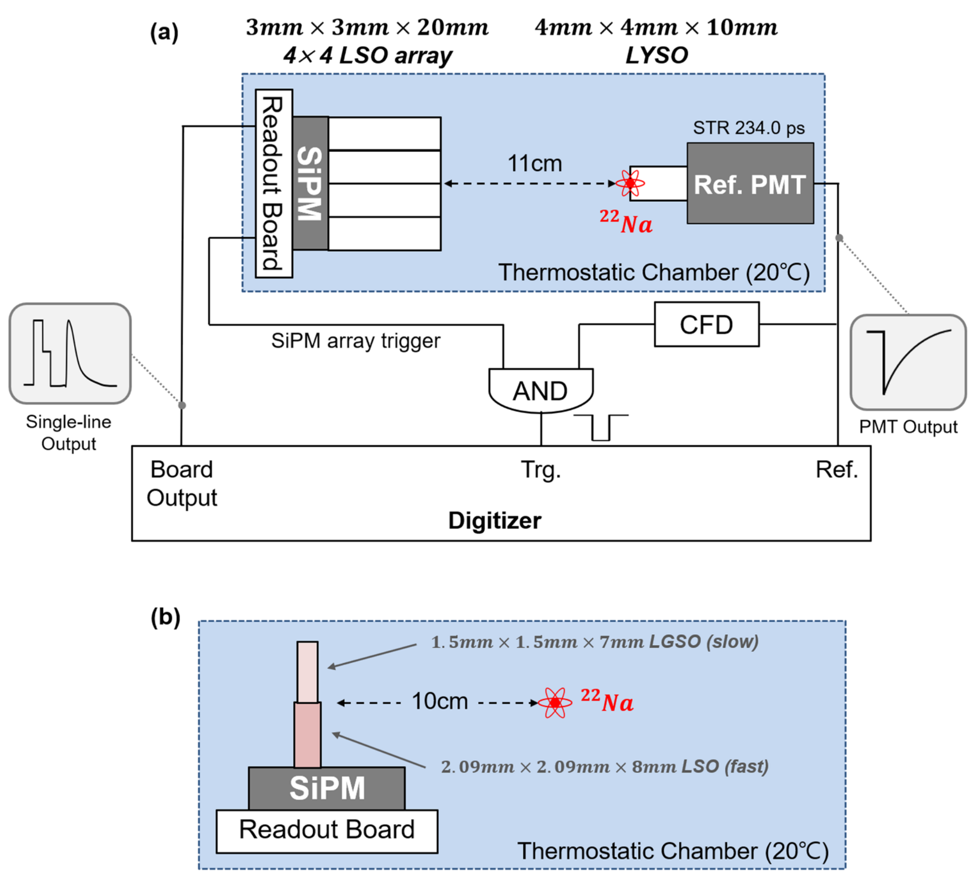

Fig. 3 Data acquisition setups **a** Coincidence detection setup, **b** Phoswich detector setup

lutetium gadolinium oxyorthosilicate (LGSO, dimension; 1.5 mm × 1.5 mm × 7 mm, τ = 60 ns, slow) crystal on an LSO crystal (dimension; 2.09 mm × 2.09 mm × 8 mm, τ = 42 ns, fast). The detector was side-irradiated by a ^{22}Na source at a distance as shown in Fig. 3b.

2.4 Data analysis

2.4.1 Positioning map and threshold levels adjustment

A positioning map was constructed by assuming the lower and the upper widths of the L-shaped tag pulse as the 2D x and y positions, respectively. We adjusted the two threshold levels to produce an optimized positioning map. Because of the non-perfectly rectangular shape of the tag pulse signal owing to its finite rising and falling time and bandwidth limitation of the electronic components, the optimal levels for width measurement need to be investigated. We defined the distance-to-width ratio (DWR) as a figure of merit for the crystal positioning map. DWR was calculated as the ratio of the separating distance between the centers of two adjacent pixels to the average full-width at half-maximum (FWHM) at the two pixels. We measured the average DWR values over the SiPM array (Eq. 1) when the low and high digital threshold voltages ranged from 100 to 300 mV and from 450 to 650 mV in steps of 25 mV, respectively. A high average DWR indicates a clear crystal separation throughout the detector area; thus, we selected a threshold pair that yielded the highest average DWR.

maximum amplitude of a SiPM signal coupled with a scintillation crystal can be considered as a function of the incident gamma ray energy E (Eq. 2), where c_1 and c_2 are constants.

$$V_{max} = c_1\left(1 - \exp\left(-c_2E\right)\right) \tag{2}$$

Because the scintillation signal timestamp detected from the low threshold included less time jitter compared to the high-level threshold timestamp owing to the fast rise time of the signal, we could fix the time interval between the rising edge time stamp and the maximum amplitude point (t_0). Then the falling edge of the scintillation signal can be modeled as an exponential decay, yielding the total dual threshold TOT value as (Eq. 3) where τ_d is a decay constant of the scintillation signal.

$$TOT = t_0 - \tau_d ln\left(\frac{V_{th,High}}{V_{max}}\right) \tag{3}$$

Therefore, the dual-threshold TOT value dependent on E can be simplified as (Eq. 4) using the properties of logarithms, where a_1, a_2, and a_3 are constants.

$$TOT(E) = a_1 + a_2 ln\left(1 - exp\left(-a_3E\right)\right) \tag{4}$$

Various radioactive sources of ^{22}Na, ^{133}Ba, ^{137}Cs with known photopeak energy values of 511 keV, 356 keV, and 662 keV respectively were used to fit the equation and inversely calculate the linear gamma ray energy value.

$$\begin{aligned} &average\ DWR = \frac{1}{N_{Hor} + N_{Ver}} \cdot \left(\sum_{(i,j)} DWR_{(i,j)} + \sum_{(m,n)} DWR_{(m,n)}\right) \\ &(i,j):\quad Horizontally\ adjacent\ pixel\ pairs \\ &(m,n):\quad Vertically\ adjacent\ pixel\ pairs \\ &N_{Hor}, N_{Ver}:\quad Number\ of\ Horizontally/Vertically\ adjacent\ pixel\ pairs \end{aligned} \tag{1}$$

2.4.2 Energy estimation

The next step was to adjust the common-cathode signal gain for energy estimation using dual thresholds. If the high threshold was set too high for the scintillation signal, the minimum acceptable energy value would have been limited. Therefore, we set the common cathode channel gain to alleviate the problem of a low dynamic range.

Moreover, we corrected the inherent energy nonlinearity of the dual-threshold TOT method [44]. The correction model was constructed considering both the SiPM saturation and dual-threshold TOT response to scintillation pulses with different energy values. The

2.4.3 Timing performance optimization

The detector timing performance was evaluated from the arrival time difference histogram obtained between the devised detector block and the reference detector with a known single time resolution (STR_{ref}) of 234 ps. The time difference histogram was constructed based only on the events of which the energy fell into a full-width at tenth-maximum (FWTM) of the 511 keV photopeak. The coincidence time resolution (CTR) of the devised block (CTR_{dev}) was calculated by quadratically subtracting the STR_{ref} from CTR measured between two detector blocks ($CTR_{dev\text{-}ref}$) and multiplying by $\sqrt{2}$.

Because each SiPM anode signal was fed into a HPF in order to achieve optimal timestamp pickoff, the slow component of the SiPM signal was suppressed. Therefore, the HPF output signal can be approximated to be proportional to $E \cdot \exp(-t/\tau_r)$, so that the logarithmic relation between different energies and arrival time pair (E_1, E_2, T_1, T_2) (Eq. 5) can be derived [49].

$$log\left(E_2/E_1\right) \propto T_2 - T_1 \tag{5}$$

Based on this relationship, the signal time walk caused by the leading-edge discriminating method with the same threshold voltage was compensated to optimize the detector timing performance. We generated a correction line on a scatter plot of $\log(E_2/E_1)$ versus (T_2–T_1) values for every pair of the coincidence events through orthogonal linear regression. The compensated CTR value was measured using corrected timing differences.

2.4.4 Decay time calculation

The decay time constant (τ_d) value was obtained from the scintillation signal following the L-shaped tag pulse and the dual thresholds. τ_d was calculated according to Eq. 6 which can be derived from simple SiPM modeling, neglecting the rise time of the scintillation signal [47].

$$\tau_d = \left(TOT_{Low} - TOT_{High}\right)/log\left(V_{th,High}/V_{th,Low}\right) \tag{6}$$

We used MATLAB R2020a for the entire data analysis and fitting procedure.

3 Results

3.1 L-shaped tag pulse properties

To determine the tag pulse widths, we examined the PWM circuit output as a function of C_W while R_W was fixed at 50 Ω. As shown in Fig. 4a and Table 1, the output pulse widths increased linearly with the selected C_W while the dispersion was kept low enough to be separated from each other. Figure 4b shows a representative output signal from the SiPM pixel D3 of the tested board. The upper pulse width was successfully varied depending on the vertical pixel position while the lower pulse width was fixed with the horizontal pixel position (Fig. 4c), and vice versa for the lower pulse width (Fig. 4d). This distinct separation led to

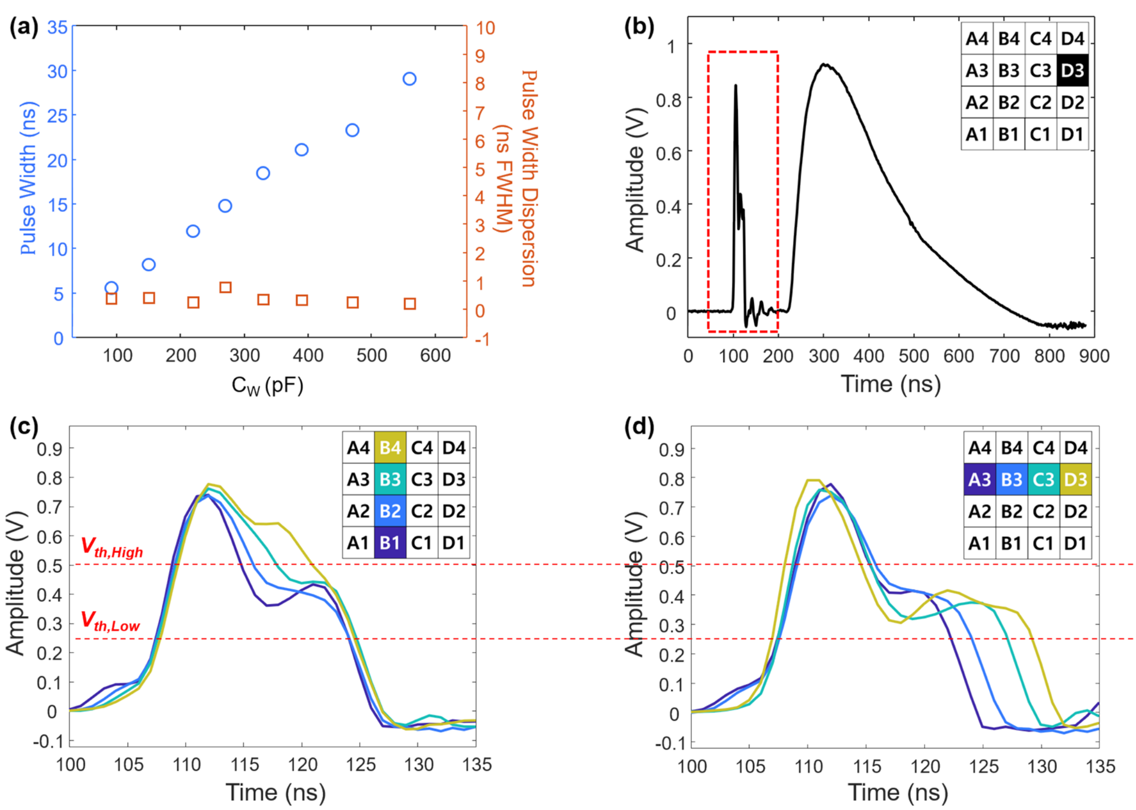

Fig. 4 L-shaped tag pulse properties. **a** PWM output property **b** Representative board output (D3). Red dashed box represents an L-shaped tag pulse **c** Vertical L-shaped pulse comparison **d** Horizontal L-shaped pulse comparison

Table 1 PWM output property

C_W (pF)	Pulse width (ns)	Pulse width dispersion (ns FWHM)
91	5.56	0.38
150	8.18	0.41
220	11.9	0.25
270	14.8	0.79
330	18.4	0.34
390	21.1	0.33
470	23.3	0.25
560	29.0	0.20

clear incident crystal identification in the positioning map (see Sect. 3.2.1).

3.2 Block detector performance

3.2.1 Positioning map

In the crystal positioning map, the 4×4 LSO crystals were clearly separated without overlaps between any pair of adjacent crystal pixels (Fig. 5a, b). The average DWR values were calculated and plotted (Fig. 5c, d). For clear crystal identification, the optimal dual threshold levels were selected as 250 mV for $V_{th,Low}$ and 500 mV for $V_{th,High}$, where the highest DWR value was measured as 15.95.

3.2.2 Dual-threshold energy estimation and correction

When the dual thresholds were used for energy estimation, the high threshold level determines the lower limit of the measured energy dynamic range. Therefore, we adjusted the common cathode signal amplifier gain to secure an energy window of at least 300 keV for the 511 keV photopeak. Subsequently, the dual-threshold TOT photopeaks of ^{22}Na, ^{133}Ba, and ^{137}Cs were measured from dual-threshold TOT energy histograms obtained from single irradiation for each SiPM pixel position. Crystal position-wise energy correction was conducted by converting the measured TOT energy values into keV units through the nonlinear fitting curves (Fig. 6a). The average energy resolution for the 511 keV gamma ray was calculated as $15.0 \pm 1.1\%$ and the energy resolution of each pixel is shown in Fig. 6b.

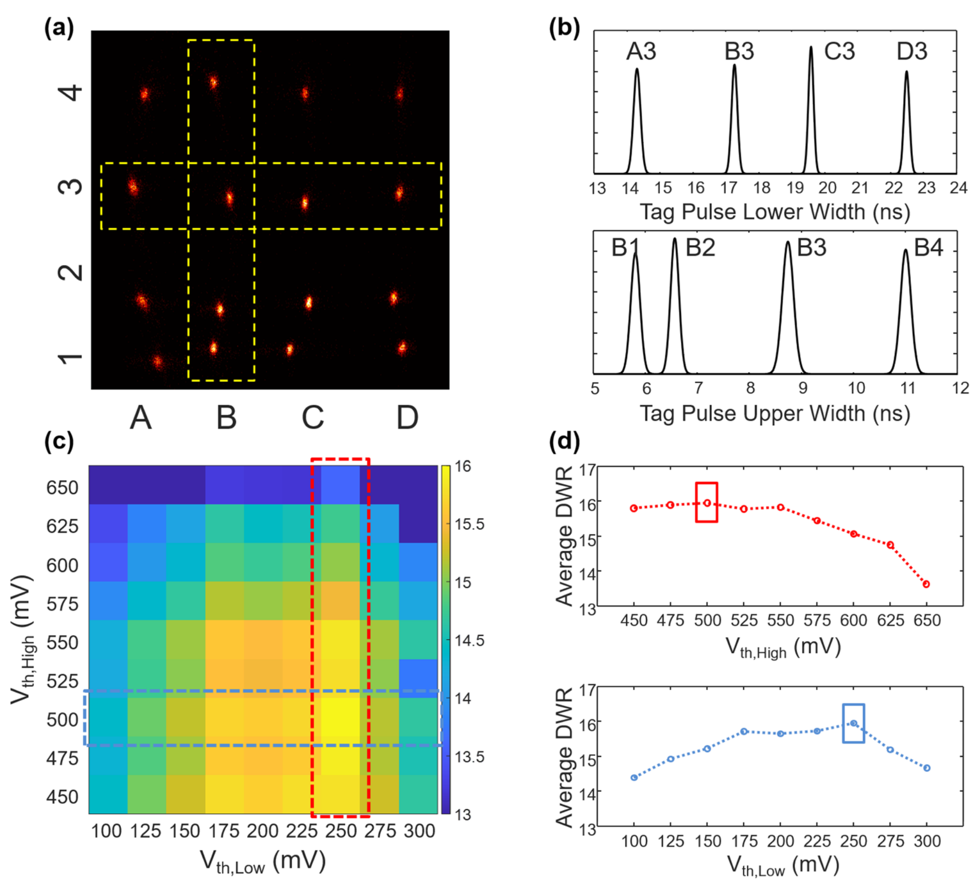

Fig. 5 Crystal Identification Performance **a** Crystal positioning map **b** Row "3" and Column "B" line profiles **c** DWR map, **d** DWR profiles ($V_{th,low} = 250$ mV fixed (red) and $V_{th,high} = 500$ mV fixed (blue))

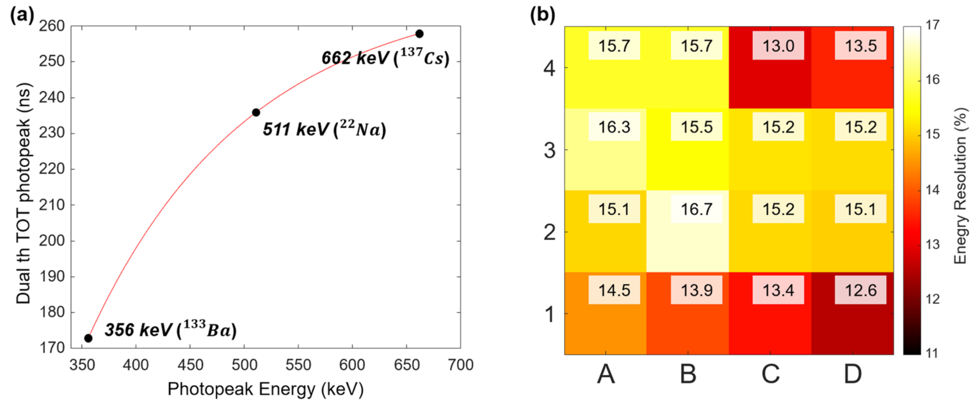

Fig. 6 Energy estimation performance **a** Energy fitting curve **b** Energy resolution map

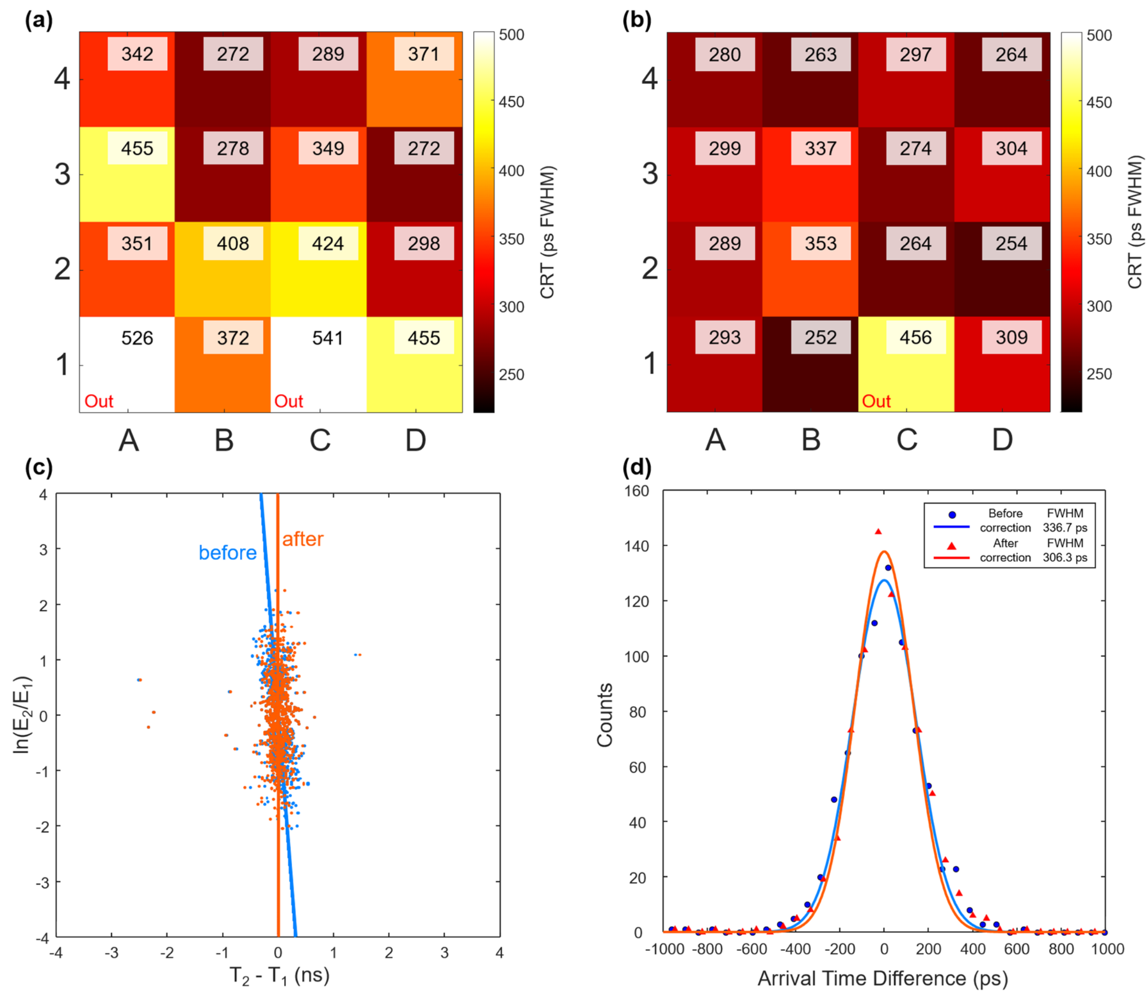

Fig. 7 **a** CTR map before time walk correction **b** CTR map after time walk correction **c** Representative time walk correction plot **d** Representative arrival time difference histogram

3.2.3 Timing performance and time walk correction

Figure 7a shows the CTR distribution of the block detector without the time walk correction. An average CTR value of 352.6 ± 65.3 ps FWHM was achieved over the SiPM array excluding the outliers. For the logarithmic 1-dimensional time walk compensation, the relationship between log(E_2/E_1) and (T_2–T_1) was obtained from the fitted line. Figure 7c shows an example obtained at the SiPM pixel A4. After the correction, the detected time difference drift due to energy variation was eliminated. Figure 7d shows a representative timing histogram before and after compensation. The CTR value improved from 336.7 ps FWHM to 306.3 ps FWHM. Throughout the detector array, an average CTR value over the SiPM array was improved to 288.7 ± 29.3 ps FWHM excluding an outlier after the compensation. The time walk compensation also flattened the CTR distribution map (Fig. 7b), reducing the variation of CTR values over the detector.

3.3 Multilayer crystal discrimination

Two pulse shapes with long and short decay time constants were clearly identified as shown in Fig. 8. The excellent discrimination performance demonstrated that the shape information of the scintillation signal was well preserved.

4 Discussion

In this study, we proposed and conducted proof-of-concept evaluation of a fully time-based position multiplexing with a single-transmission-line output. Because the digital pulse output from each PWM circuit has finite rising and falling time and its effect is accumulated during the analog summing stage, a careful consideration in selecting the $V_{th,High}$ and $V_{th,Low}$ to measure the pulse widths. The DWR played an important role as a figure of merit to determine the optimal levels with clear incident crystal identification.

One advantage of the proposed fully time-based position multiplexing is the simple rejection of the inter-crystal scattering (ICS) of 511 keV gamma rays. As we estimated the energy from the common-cathode signal, where the output signals from 16 SiPM cathodes were summed together, a simple energy window cannot efficiently discriminate signal detection from multiple positions due to ICS events. Improper handling of ICS events results in positioning errors and difficulties in crystal identification. However, in our proposed method, because the summing stage stacks the position tag pulse signals from all active row or column pulses, positioning errors caused by ICS events can be discarded simply by applying a threshold higher than twice the height of a single pulse.

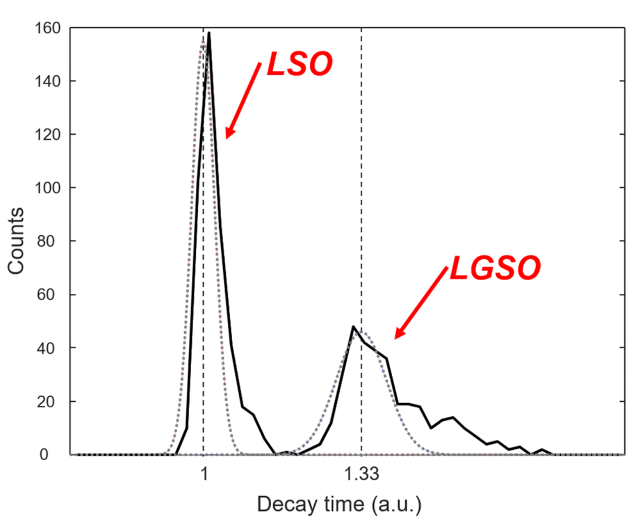

Fig. 8 Phoswich detector crystal distinguishment

Although we constructed a detector based on SiPMs one-to-one coupled to identical pitch-sized scintillation crystals, the optical grease smearing and minor mismatches between the crystal array and SiPM array made it difficult to set the reference voltage of the leading-edge discriminator for the individual anode signal to be sufficiently low. Signal thresholding with a reference voltage not low enough led to sub-optimal timing performance throughout the detector array. However, we achieved an average detector CTR performance of sub-300 ps FWHM after a time walk correction by employing the logarithmic relationship between energy and the detected arrival time. Time walk compensation methods using polynomial 2D fitting or artificial neural networks would also work well with at least a 10% improvement in timing performance [49]. If we exploit delayed AND-logic to add a simple false event-discriminating circuit stage after the digitization of individual SiPM anode signals, undesirable interference between adjacent pixels can be minimized. Accordingly, the reference voltage can be sufficiently lowered to a level of a few early photons to achieve optimal timing performance.

From the PWM circuit evaluation, the pulse width can be linearly modulated by varying the capacitance value with susceptible dispersion leaving considerable room to choose from. Therefore, by simply modulating passive element values, the proposed multiplexing method can easily be extended to a large-area detector, for example, an 8 × 8 SiPM array. As the arrival time information was individually encoded at the rising edge of the position tag pulse signal at each SiPM anode channel, the increased multiplexing ratio would not worsen the detector timing performance. However, as the detector sensitivity increases proportionally with the detector area, the detector counting performance of a detector with a larger area would be degraded at high count rate. Therefore, high-speed circuit implementation and optimal selection of position tagging pulse widths and scintillation signal delay would be required to mitigate the counting performance degradation.

We showed that a well-preserved scintillation signal shape leads to DOI feasibility through a phoswich detector setup investigation. The exceptional discriminating performance will also be helpful in the identification and rejection of cross-layer-crystal scatter (CLCS) events in phoswich detectors with crystal pairs such as LSO/LYSO,

LYSO/BGO, or LSO/$LaBr_3$ [50]. A large number of crystal layers with different pulse shapes would considerably enhance the imaging quality, but it should also be pointed out that the DOI resolution is limited to the layer thickness. Continuous DOI encoding with a phosphor-coated detector is another possible approach [51, 52]. On the other hand, the pulse shape information enables the exploitation of side-to-side phoswich detector structures, leading to further improvement in spatial resolution [53–55]

The data acquisition and analysis for the feasibility evaluation in this study was conducted with the DRS4 based data acquisition setup accompanied by in-silico MATLAB analysis. The waveform samples from the detectors were digitized by the DRS4 based digitizer with sampling rate of 1 GSPS. The in-silico analysis was conducted with signal data having a time bin of 20 ps by 50 times oversampling using cubic interpolation to reduce the quantization error. Instead, we can utilize a dual-phase tapped-delay-line TDC along with on-the-fly time bin calibration to ultimately make use of temporally encoded signal data. The TDC architecture provides a timestamp detection resolution of approximately 10 ps by continuous fine time calibration using the most up-to-date bin widths [56–59]. The fine-time-bin TDC architecture implemented in FPGA enables the scale-up of the proposed time-based readout method to a system level with negligible performance degradation and low DAQ bulkiness at an affordable cost.

5 Conclusions

We proposed and successfully demonstrated a time-based single transmission-line readout method along with dual thresholds based on a one-to-one LSO crystal-coupled SiPM array. Particularly, we demonstrated the feasibility of decoding the 3D gamma ray interaction position with a single-line readout. Scintillation signal properties including energy and timing information were also well encoded in the temporal signals showing promising TOF capability.

Funding This work was supported by the Korea Medical Device Development Fund grant funded by the Korea government (the Ministry of Science and ICT, the Ministry of Trade, Industry and Energy, the Ministry of Health & Welfare, the Ministry of Food and Drug Safety) (Project Number: KMDF_PR_20200901_0028, 9991007087) and grants from the National Research Foundation of Korea (NRF) funded by the Korean Ministry of Science and ICT (Grant No. 2020M2D9A1093989).

Declarations

Conflict of interest The authors declare that they have no conflict of interest.

Ethical approval This article does not contain any studies with human participants or animals performed by any of the authors.

References

1. Lee JS, et al. Geiger-mode avalanche photodiodes for PET/MRI. In: Iniewski K, editor., et al., Electronics for radiation detection. Boca Raton: CRC Press; 2010. p. 179–200.
2. Kwon SI, et al. Development of small-animal PET prototype using silicon photomultiplier (SiPM): initial results of phantom and animal imaging studies. J Nucl Med. 2011;52(4):572–9.
3. Yamaya T, et al. A SiPM-based isotropic-3D PET detector X'tal cube with a three-dimensional array of 1 mm^3 crystals. Phys Med Biol. 2011;56(21):6793.
4. Roncali E, et al. Application of silicon photomultipliers to positron emission tomography. Ann Biomed Eng. 2011;39(4):1358–77.
5. Ferri A, et al. Performance of FBK high-density SiPM technology coupled to Ce:LYSO and Ce:GAGG for TOF-PET. Phys Med Biol. 2014;59(4):869.
6. Casey M, et al. A next generation SiPM based PET/CT system with improved time and spatial resolution. J. Nucl. Med. 2017;58:1332S.
7. Lee MS, et al. Prototype pre-clinical PET scanner with depth-of-interaction measurements using single-layer crystal array and single-ended readout. Phys Med Biol. 2017;62(10):3983.
8. Hsu DF, et al. Studies of a next-generation silicon-photomultiplier–based time-of-flight PET/CT system. J Nucl Med. 2017;58(9):1511–8.
9. Won JY, et al. Development and initial results of a brain PET insert for simultaneous 7-tesla PET/MRI using an FPGA-only signal digitization method. IEEE Trans Med Imaging. 2021;40(6):1579–90.
10. Cates JW, et al. Analytical calculation of the lower bound on timing resolution for PET scintillation detectors comprising high-aspect-ratio crystal elements. Phys Med Biol. 2015;60(13):5141.
11. Nemallapudi MV, et al. Sub-100 ps coincidence time resolution for positron emission tomography with LSO:Ce co-doped with Ca. Phys Med Biol. 2015;60(12):4635.
12. Gundacker S, et al. Measurement of intrinsic rise times for various L (Y) SO and LuAG scintillators with a general study of prompt photons to achieve 10 ps in TOF-PET. Phys Med Biol. 2016;61(7):2802.
13. Gundacker S, et al. State of the art timing in TOF-PET detectors with LuAG, GAGG and L (Y) SO scintillators of various sizes coupled to FBK-SiPMs. J Instrum. 2016;11(08):P08008.
14. Brunner SE, et al. BGO as a hybrid scintillator/Cherenkov radiator for cost-effective time-of-flight PET. Phys Med Biol. 2017;62(11):4421.
15. Cates JW, et al. Improved single photon time resolution for analog SiPMs with front end readout that reduces influence of electronic noise. Phys Med Biol. 2018;63(18):185022.
16. Dey S, et al. A CMOS ASIC design for SiPM arrays. In: IEEE nuclear science symposium conference record. 2011. p. 732–737.
17. Dolinsky S, et al. Timing resolution performance comparison for fast and standard outputs of SensL SiPM. In: 2013 IEEE nuclear science symposium and medical imaging conference. NSS/MIC; 2013. pp 1–6.
18. Brunner SE, et al. A comprehensive characterization of the time resolution of the Philips digital photon counter. J Instrum. 2016;11(11):P11004.
19. Yoshino M, et al. Development and performance evaluation of time-over-threshold based digital PET (TODPET2) scanner

using SiPM/Ce: GAGG-arrays for non-invasive measurement of blood RI concentrations. J Instrum. 2017;12(02):C02028.
20. Chen Y, et al. DIET: a multi-channel SiPM readout ASIC for TOF-PET with individual energy and timing digitizer. J Instrum. 2018;13(07):07023.
21. Shimazoe K, et al. Development of simultaneous PET and Compton imaging using GAGG-SiPM based pixel detectors. Nucl Instrum Methods Phys Res Sect A Accel Spectrom Detect Assoc Equip. 2020;954:161499.
22. Olcott PD, et al. Compact readout electronics for position sensitive photomultiplier tubes. IEEE Trans Nucl Sci. 2005;52(1):21–7.
23. Popov V, et al. A novel readout concept for multianode photomultiplier tubes with pad matrix anode layout. Nucl Instrum Methods Phys Res Sect A Accel Spectrom Detect Assoc Equip. 2006;567(1):319–22.
24. Ito M, et al. Continuous depth-of-interaction measurement in a single-layer pixelated crystal array using a single-ended readout. Phys Med Biol. 2013;58(5):1269.
25. Dey S, et al. A row-column summing readout architecture for SiPM based PET imaging systems. In: 2013 IEEE nuclear science symposium and medical imaging conference. NSS/MIC; 2013. pp. 1–5.
26. Kwon SI, et al. Signal encoding method for a time-of-flight PET detector using a silicon photomultiplier array. Nucl Instrum Methods Phys Res Sect A Accel Spectrom Detect Assoc Equip. 2014;761:39–45.
27. Stolin AV, et al. Evaluation of imaging modules based on SensL array SB-8 for nuclear medicine applications. IEEE Trans Nucl Sci. 2014;61(5):2433–8.
28. Siegel S, et al. Simple charge division readouts for imaging scintillator arrays using a multi-channel PMT. IEEE Trans Nucl Sci. 1996;43(3):1634–41.
29. Goertzen AL, et al. Design and performance of a resistor multiplexing readout circuit for a SiPM detector. IEEE Trans Nucl Sci. 2013;60(3):1541–9.
30. Ko GB, et al. Development of a front-end analog circuit for multichannel SiPM readout and performance verification for various PET detector designs. Nucl Instrum Methods Phys Res Sect A Accel Spectrom Detect Assoc Equip. 2013;703:38–44.
31. Downie E, et al. Investigation of analog charge multiplexing schemes for SiPM based PET block detectors. Phys Med Biol. 2013;58(11):3943.
32. Olcott PD, et al. Cross-strip multiplexed electro-optical coupled scintillation detector for integrated PET/MRI. IEEE Trans Nucl Sci. 2013;60(5):3198–204.
33. Powolny F, et al. A novel time-based readout scheme for a combined PET-CT detector using APDs. IEEE Trans Nucl Sci. 2008;55(5):2465–74.
34. Orita T, et al. A new pulse width signal processing with delay-line and non-linear circuit (for ToT). Nucl Instrum Methods Phys Res Sect A Accel Spectrom Detect Assoc Equip. 2011;648:S24–7.
35. Olcott PD, et al. Pulse width modulation: a novel readout scheme for high energy photon detection. In: 2008 IEEE nuclear science symposium conference record. 2008. pp. 4530–4535.
36. Schmand M, et al. Performance results of a new DOI detector block for a high resolution PET-LSO research tomograph HRRT. IEEE Trans Nucl Sci. 1998;45(6):3000–6.
37. Pepin CM, et al. Properties of LYSO and recent LSO scintillators for phoswich PET detectors. IEEE Trans Nucl Sci. 2004;51(3):789–95.
38. Schmall JP, et al. Characterization of stacked-crystal PET detector designs for measurement of both TOF and DOI. Phys Med Biol. 2015;60(9):3549.
39. Yamamoto S, et al. Timing performance measurements of Si-PM-based LGSO phoswich detectors. Nucl Instrum Methods Phys Res Sect A Accel Spectrom Detect Assoc Equip. 2016;821:101–8.
40. Fujiwara T, et al. Multi-level time-over-threshold method for energy resolving multi-channel systems. IEEE Trans Nucl Sci. 2010;57(5):2545–8.
41. Parl C, et al. Fast charge to pulse width converter for monolith PET detector. IEEE Trans Nucl Sci. 2012;59(5):1809–14.
42. Shimazoe K, et al. Dynamic time over threshold method. IEEE Trans Nucl Sci. 2012;59(6):3213–7.
43. Bieniosek MF, et al. Compact pulse width modulation circuitry for silicon photomultiplier readout. Phys Med Biol. 2013;58(15):5049.
44. Grant AM, et al. A new dual threshold time-over-threshold circuit for fast timing in PET. Phys Med Biol. 2014;59(13):3421.
45. Yonggang W, et al. A linear time-over-threshold digitizing scheme and its 64-channel DAQ prototype design on FPGA for a continuous crystal PET detector. IEEE Trans Nucl Sci. 2014;61(1):99–106.
46. Ko GB, et al. Time-based signal sampling using sawtooth-shaped threshold. Phys Med Biol. 2019;64(12):125020.
47. Ota R. Development of dual time-over-threshold method for estimation of scintillation decay time and energy. In: Proceedings of the second international symposium on radiation detectors and their uses. ISRD; 2018. p. 011012.
48. Ko GB, et al. Single transmission-line readout method for silicon photomultiplier based time-of-flight and depth-of-interaction PET. Phys Med Biol. 2017;62(6):2194.
49. Xie S, et al. Methods to compensate the time walk errors in timing measurements for PET detectors. IEEE Trans Radiat Plasma Med Sci. 2020;4(5):555–62.
50. Prout DL, et al. A digital phoswich detector using time-over-threshold for depth of interaction in PET. Phys Med Biol. 2020;65(24):245017.
51. Du H, et al. Continuous depth-of-interaction encoding using phosphor-coated scintillators. Phys Med Biol. 2009;54(6):1757.
52. Berg E, et al. A combined time-of-flight and depth-of-interaction detector for total-body positron emission tomography. Med Phys. 2016;43(2):939–50.
53. Han SK, et al. Simulation study of side-by-side phoswich PET detector configuration for providing high spatial resolution of< 0.4 mm. In: 2018 Joint 10th international conference on soft computing and intelligent systems (SCIS) and 19th international symposium on advanced intelligent systems (ISIS). IEEE; 2018. pp. 346–349.
54. Wei Q, et al. A side-by-side LYSO/GAGG phoswich detector aiming for SPECT imaging. Nucl Instrum Methods Phys Res Sect A Accel Spectrom Detect Assoc Equip. 2020;953:163.
55. Wei Q, et al. A position sensitive scintillation detector using a side-by-side GAGG-F/GAGG-T phoswich block. J Instrum. 2020;15(04):T04001.
56. Won JY, et al. Dual-phase tapped-delay-line time-to-digital converter with on-the-fly calibration implemented in 40 nm FPGA. IEEE Trans Biomed Circuits Syst. 2015;10(1):231–42.
57. Won JY, et al. Time-to-digital converter using a tuned-delay line evaluated in 28-, 40-, and 45-nm FPGAs. IEEE Trans Instrum Meas. 2016;65(7):1678–89.
58. Won JY, et al. Highly integrated FPGA-only signal digitization method using single-ended memory interface input receivers for time-of-flight PET detectors. IEEE Trans Biomed Circuits Syst. 2018;12(6):1401–9.
59. Won JY, et al. Comparator-less PET data acquisition system using single-ended memory interface input receivers of FPGA. Phys Med Biol. 2020;65(15):155.